Deconvoluting charge-transfer, mass transfer, and ohmic resistances in phosphonic acid-sulfonic acid ionomer binders used in electrochemical hydrogen pumps

Karthik Arunagiri[1], Andrew Jark-Wah Wong[1], Luis Briceno-Mena[2], Hania Mohamed Gaber Hassan Elsayed [1], José A. Romagnoli[2], Michael J. Janik[1], and Christopher G. Arges[1]*

[1]Department of Chemical Engineering, The Pennsylvania State University, University Park, PA, 16802, USA
[2]Cain Department of Chemical Engineering, Louisiana State University, Baton Rouge, LA, 70803, USA
*Corresponding author: cga5126@psu.edu

Abstract

Ion-pair high-temperature polymer electrolyte membranes (HT-PEMs) paired with phosphonic acid ionomer electrode binders have substantially improved the performance of HT-PEM electrochemical hydrogen pumps (EHPs) and fuel cells. Blending poly(pentafluorstyrene-*co*-tetrafluorostyrene phosphonic acid) (PTFSPA) with Nafion^{TM}, and using this blend as an electrode binder, improved proton conductivity in the electrode layer resulting in a 2 W cm^{-2} peak power density of fuel cells at 240 °C (a HT-PEM fuel cell record). However, much is unknown about how phosphonic acid ionomers blended with perfluorosulfonic acid materials affect electrode kinetics and gas transport in porous electrodes. In this work, we studied the proton conductivity, electrode kinetics, and gas transport resistances of 3 types of phosphonic acid ionomers, poly(vinyl phosphonic acid), poly(vinyl benzyl phosphonic acid), and PTFSPA by themselves and when blended with Aquivion® (a perfluorosulfonic acid material). These studies were performed using EHP platforms. For all phosphoric acid ionomer types, the addition of Aquivion® promoted ionic conductivity, hydrogen oxidation/evolution reaction kinetics (HOR/HER), and hydrogen gas permeability. Solid-state ^{31}P NMR revealed that the addition of Aquivion® eliminated or significantly reduced phosphate ester formation in phosphoric acid

ionomers and this plays a vital role in enhancing ionomer blend conductivity. Using the best blend variant, PTFSPA-Aquivion®, an EHP performance of 5.1 A cm^{-2} at 0.4 V at T = 200 °C was attained. Density functional theory (DFT) calculations identified that phosphonic acids with electron-withdrawing moieties reduced the propensity of the phosphonic acid to specifically adsorb on platinum electrocatalyst surfaces. The relative adsorption affinity of the various phosphonic acid ionomers from DFT is consistent with an experimentally obtained charge transfer resistance. A voltage loss breakdown model revealed that the addition of Aquivion® reduced activation and concentration overpotentials in EHPs. Overall, a systematic experimental and modeling approach provided further insight as to how perfluorosulfonic acid ionomers blended with phosphoric acid ionomers affect ionic conductivity, reaction kinetics, and gas permeability in EHP platforms.

Broader context

Electrochemical hydrogen pumps (EHPs) using a polymeric proton exchange membrane (PEM) is an enticing technology for separating hydrogen from gas mixtures and compressing the purified hydrogen. This platform is conducive for distributing hydrogen in the natural gas pipeline in addition to hydrogen compression at fueling stations and hydrogen recovery in industrial processes. Low-temperature EHPs (below 100°C) using Nafion™ as the PEM is the most mature EHP technology; however, it requires gas humidification to operate and is very sensitive to contaminants in the gas feed. Recently, we have demonstrated ion-pair-based high-temperature PEM (HT-PEM) paired with a fluorinated styrene-based phosphonic acid ionomer electrode binder for purifying hydrogen gas at 1 A cm^{-2} from heavy carbon monoxide mixtures (e.g., 40mol%). Central to this achievement was the selection of the electrode binder material. Most HT-PEM EHP

systems to date have used poly(tetrafluoroethylene) (PTFE) binder imbibed with phosphoric acid. These electrodes have high platinum loadings and poor performance due to the presence of liquid phosphoric acid. There are significant knowledge gaps as to how electrode binder ionomer chemistry affects EHP performance. In this study, a comprehensive framework spanning experiments and computation methods was deployed to study how phosphonic acid ionomers and phosphonic acid ionomers blended with perfluorosulfonic acid ionomers affect HT-PEM electrode kinetics, proton conductivity, and hydrogen diffusivity in EHPs. Excellent HT-PEM EHP performance, 5.1 $A.cm^{-2}$ at 0.4 V, was attained when using poly(pentafluorostyrene-*co*-tetrafluorostyrene phosphonic acid) (PTFSPA) blended with Aquivion® as the electrode binder.

Introduction

Hydrogen will play a central role in decarbonizing the global economy in the coming years. About 10% of carbon dioxide (CO_2) emissions hail from steel and ammonia manufacturing [1, 2]. Green hydrogen can be used as an alternative reducing agent in steel manufacturing as opposed to carbon monoxide (CO) derived from fossil fuels[3]. The Haber-Bosch process for ammonia production (for manufacturing fertilizer) utilizes hydrogen produced from steam-reformed natural gas[4]. These are two notable examples of where green hydrogen can be used to clean up hard-to-abate manufacturing sectors of the economy. Furthermore, hydrogen has the potential to be a cost-effective energy storage medium for long-term/seasonal energy storage[5] and the fuel of choice for heavy-duty vehicle (HDV) transport[6]. The energy requirements for HDV transport are commensurate to the range of the vehicle and weight of the vehicle (i.e., fuel cells display higher energy density over battery electric vehicles when the energy requirement exceeds 80 kWh)[7,8].

Given hydrogen's central role in decarbonization, the U.S. Department of Energy has emphasized an important research goal related to hydrogen: reducing the cost of hydrogen production to $1 per kg of hydrogen within 1 decade[9]. Apart from the production cost for green hydrogen, which hovers around $5 kg^{-1}, another impediment to the widespread proliferation of hydrogen is its delivery and dispensing costs. Elgowainy *et al.* have shown that current hydrogen costs delivered via gaseous tube trailers or liquid tankers are about $3 kg^{-1} [10]. Melaina *et al.* calculated that the delivery and dispensing costs amount to $8 kg^{-1} [11]. These two studies highlight that the cost of hydrogen delivery and dispensing are on par with or exceed today's current green hydrogen production costs. Making hydrogen economically appealing for the energy and industrial sectors necessitates a reduction in delivery costs in addition to production costs.

Piped transport is often the most cost-effective way to transport gases [12]. This is one reason why the United States of America has an extensive pipeline for the transport and delivery of natural gas. Building out a new pipeline network for transporting and delivering hydrogen is a timely endeavor, and the timeline for hydrogen adoption in the economy will be fast over the coming decade. Thus, it has been proposed to use the existing natural gas pipeline to transport hydrogen for alleviating hydrogen transport costs and to promote hydrogen adoption[13, 14]. However, there are a myriad of issues that need to be addressed before using the natural gas pipeline for hydrogen storage and delivery. The main issues are the embrittlement of pipeline materials with hydrogen, hydrogen leakage from the pipeline, and the ability to pressure and move hydrogen within the pipeline[15]. The U.S. Department of Energy's Office of Hydrogen and Fuel Cell Technologies Office has created the HyBlend Initiative to examine and address the technical barriers to blend hydrogen in the natural gas pipeline[13]. The embrittlement of pipeline materials with hydrogen is a key issue [15]. This concern is addressed by diluting hydrogen with natural gas to 20% less,

preferably 3 to 10%. Hydrogen can be burned along with the blended natural gas when distributed to the endpoints in the pipeline; however, this is not a good use of electrolytically produced green hydrogen. Additionally, many applications that use hydrogen, such as fuel cells and industrial operations, need high purity of hydrogen (i.e., >99% pure) and compression of hydrogen. An electrochemical hydrogen pump (EHP) is a compelling technology for purifying the hydrogen from the natural gas-hydrogen mixture in addition to compressing the purified hydrogen simultaneously[16]. Other methods for hydrogen separation include pressure swing adsorption[17], and membranes based on palladium[18] and graphenylene[19], but these separation techniques require a downstream compressor for hydrogen compression.

At the heart of an EHP is a membrane electrode assembly (MEA). The anode in the MEA performs the electrochemical hydrogen oxidation reaction (HOR) that generates two electrons and two protons. The protons migrate across a polymeric proton exchange membrane (PEM) while the electrons generated at the anode move externally through the cell and meet up with the protons and the electrons to recombine at the cathode through an electrochemical reduction reaction (i.e., hydrogen evolution reaction (HER)). The other gas species fed into the anode with the hydrogen do not permeate across the PEM and exit the anode. The purity of the formed hydrogen at the cathode is over 99%[20, 21]. A small amount of the other gas components can seep across the PEM, but engineering the PEM chemistry and making it thicker can mitigate the gas crossover. The PEM separator allows the produced hydrogen at the cathode to be pressurized. **Figure 1a** conveys the EHP platform.

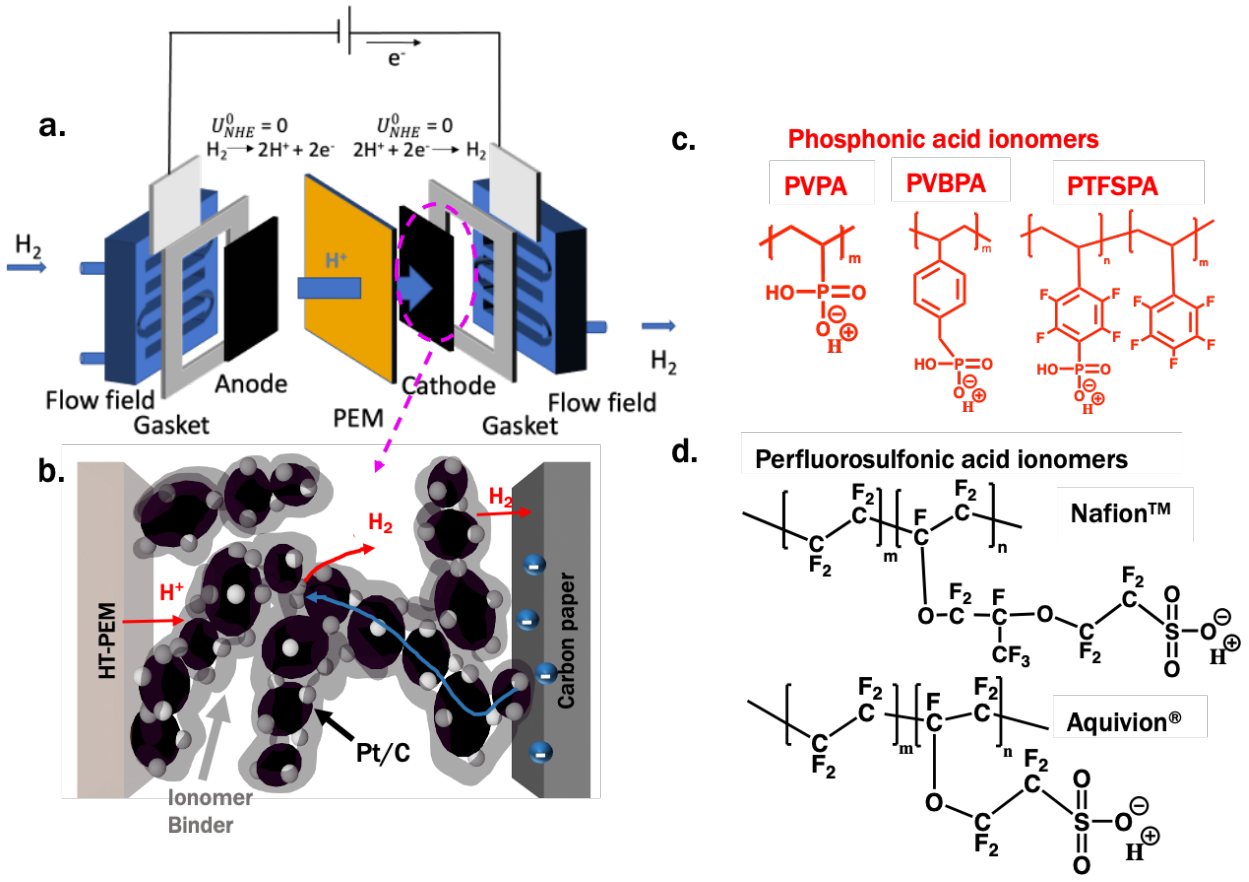

Figure 1. (a) A schematic diagram of an electrochemical hydrogen pump (EHP). (b) A magnified depiction of an EHP cathode with an electrode ionomer binder illustrating proton and electron transport, the HER reaction, and hydrogen gas transport; Chemical structures of various binder materials used in this work: (c) phosphonic acid ionomers and (d) perfluorosulfonic acid ionomers.

The first generation of EHPs[22] was developed by General Electric that used perfluorosulfonic acid (PFSA) PEMs, and they operated at low temperatures (< 100 °C) as the PFSA PEMs need condensed water to mediate proton conductivity. However, the low-temperature operation of EHPs makes them susceptible to irreversible performance loss when contaminants, like carbon monoxide (CO), are present in the feed gas stream[23] because CO poisons the platinum electrocatalyst[24]. Increasing the temperature to 160 °C or greater permits toleration of CO contaminants. High-temperature polymer electrolyte membranes (HT-PEMs) can be used in elevated temperature EHPs as they can provide adequate electrolyte conductivity in the

temperature range of 100 to 250 °C[21] without humidification. HT-PEMs often include phosphoric acid-imbibed polybenzimidazole (PBI) or phosphoric acid-imbibed polycations (or polycation/PBI blends)[25-27].

Our previous work[20, 25, 27] demonstrated effective HT-PEM EHP performance with a variety of hydrogen gas feed streams and employing a polycation-PBI phosphoric acid imbibed HT-PEM (aka, ion-pair HT-PEM). The electrodes used a phosphonic acid ionomer binder, i.e., poly(pentafluorostyrene-co-tetrafluorostyrene-4-phospohnic acid) (PTFSPA). These materials enabled the purification of hydrogen from heavy CO mixtures (e.g., syngas with 40% CO and a reformate mixture that contained 25% CO[20]) using an EHP. The ion-pair HT-PEM with PTFSPA electrode binders is a relatively new class of materials that have enhanced HT-PEM electrochemical systems – which also include fuel cells in addition to EHPs. Kim and co-workers demonstrated further gains in HT-PEM fuel cell performance when blending PTFSPA material (also called PWN-70) with Nafion™ for use as the electrode binder[28]. Their work attributed the improvement in power density to higher ionic conductivity in the electrode layer as Nafion™ (a PFSA material) protonates the PTFSPA and prevents PTFSPA anhydride formation. However, no consideration was given to how the addition of PFSA material to PTFSPA affects electrode kinetics and gas transport.

This work investigates ohmic, charge-transfer kinetics, and mass transfer resistances in HT-PEM EHP porous electrodes and thin films with phosphonic acid ionomers and phosphonic acid-PFSA ionomer blends. Using thin film interdigitated electrode arrays (IDAs), we show that the addition of sulfonic acid ionomers, such as Aquivion® (i.e., a short-side chain PFSA variant) and Nafion™ enhances ionomer proton conductivity. Solid-state ^{31}P NMR revealed that Aquivion® PFSA reduced, or eliminated, anhydride formation in phosphonic acid ionomers upon

an aggressive thermal annealing treatment intended to induce anhydride formation. In MEA studies, EHP polarization was reduced when Aquivion® was added to the phosphonic acid ionomer for use as electrode binders. Electrochemical impedance spectroscopy (EIS) revealed that Aquivion® reduced charge-transfer kinetic resistances as well as diffusion-related resistances. An MEA consisting of an ion-pair HT-PEM and electrodes that used PTFSPA blended with Aquivion® as the binder displayed 5.1 A cm^{-2} at 0.4 V at T = 200 °C with a pure hydrogen feed - the highest current density value in the HT-PEM EHP literature. An electrode binder composed of PVPA blended with Aquivion®, which are both commercially available materials, gave 2.25 A cm^{-2} at 0.5 V in a HT-PEM EHP with a pure hydrogen feed. This latter example shows that commercially available materials can achieve decent EHP performance. A voltage loss breakdown model[29] was used to determine the overpotentials related to reaction kinetics and hydrogen mass transfer in the porous electrodes as a function of cell current density for the various electrode ionomer binder materials. DFT simulations identified scaling trends between the propensity of the phosphonic acid and sulfonic acid groups to adsorb on platinum. The equilibrium adsorption potential, indicating the propensity of the ionomer to adsorb on the platinum catalyst, correlates well with experimentally determined charge-transfer resistances. Overall, a computational and experimental framework was deployed to deconvolute the ohmic, charge-transfer kinetics, and mass-transfer resistance contributions for HT-PEM electrode binders.

Results and discussion

Figure 1b depicts a porous electrode in a HT-PEM EHP that accentuates the electrode ionomer binder. The protons and electrons for the HOR and HER reactions in the porous electrodes need to intersect at the platinum electrocatalyst – which can be partially covered by the electrode

binder. The minimum cell voltage for the EHP if the fugacity of hydrogen on the anode and cathode are the same is 0 V. However, the practical operation of the EHP still necessitates applied potential due to various overpotentials related to reaction kinetics, ohmic losses, and hydrogen mass transfer resistances. The goal of this work was to understand how the electrode binder and binder blends affect these resistances in HT-PEM EHP porous electrodes.

Figure 1c and d depicts the chemical structures of the electrode ionomer binder candidates tested in this study. Several experiments were performed by blending phosphonic acid ionomers with perfluorosulfonic acid ionomers. Before explaining the experimental design, we review the background of binders used in HT-PEM EHPs and fuel cells. Phosphoric acid and phosphonic acid electrolytes are the electrolytes of choice for HT-PEM EHPs for purifying gases that contain no water – which is often the case for purifying hydrogen from reformed hydrocarbons or purifying hydrogen when blended with natural gas. Under neat conditions, phosphoric acid has the highest ionic conductivity of any acid[30]. Most commercial HT-PEM EHPs, as well as HT-PEM fuel cells, use poly(tetrafluoroethylene) (PTFE) electrode binders with phosphoric acid (e.g., the electrodes in BASF Celtec®'s technology, as shown in **Table 2**). Adding liquid phosphoric acid to the electrode that contains platinum nanoparticles on graphitic carbon supports (Pt/C) is detrimental to electrode performance. The phosphonate anions in the liquid acid can adsorb and poison the electrocatalyst and the large concentration of acid can foster electrode corrosion under applied potentials[31]. Substituting the PTFE and liquid acid with a phosphonic acid ionomer reduces electrocatalyst poisoning as the phosphonate groups in the ionomer are fewer than the liquid acid and tethering the phosphonate to the polymer backbone reduces the propensity for adsorption to the electrocatalyst surface[27, 32]. Removal of the liquid acid from the electrode layers also promotes gas transport. Hence, substituting phosphoric acid with phosphonic ionomers acid resolves many

of the problems of liquid phosphoric acid in electrodes with the PTFE binder. One drawback of using phosphonic acid ionomers is their proclivity to anhydride formation[32, 33] – especially those that do not have adjacent moieties that are electron-withdrawing to increase the acidity of phosphonate. The only acceptable phosphonic acid ionomer to date for HT-PEM EHPs and fuel cells is PTFSPA. As we will show later, PTFSPA is still prone to anhydride formation and its proton conductivity can be improved with the addition of a PFSA material like Aquivion®.

Although ionic conductivity in the electrode is important, we hypothesized at the onset of this work that the addition of a PFSA ionomer to a phosphonic acid ionomer in the electrode would i.) enhance HOR/HER kinetics as the PFSA is more acidic than the phosphonic acid and greater acidity promotes HOR/HER kinetics and ii.) promote hydrogen gas transport as it has been shown in low-temperature fuel cells that PFSA polymers have higher oxygen gas permeability than hydrocarbon variants[34]. **Figures 1c and 1d** and **Table 1** present the type of ionomer binder and ionomer binder blends tested in this work. **Table 1** also provides the ion exchange capacity (IEC) of the individual ionomers and the P/S ratio for the blended phosphonic acid and sulfonic acid ionomers studied. This Table also gives the amount of anhydride formed with phosphonic acid ionomers and phosphonic acid ionomers blended with Aquivion® after an aggressive thermal annealing treatment, and the maximum thin film conductivity values of the various ionomers and ionomer blends.

Table 1. The IEC values of ionomers, P/S ratio of phosphonic acid and sulfonic acid ionomer blends, and the maximum thin film ionic conductivity values of the ionomers and ionomer blends.

Material	IEC ($mmol.g^{-1}$)[a]	P/S ratios	Anhydride formation (%)[b]		Maximum thin film proton conductivity ($mS.cm^{-1}$)[c]	
			No Aquivion®	With Aquivion®	No Aquivion®	With Aquivion®
PTFSPA	1.56	0.5, 1.0, 1.6, 2.0, 4.7	21.2	0	18.2	42.5
PVPA	6.80	1.0, 2.0, 4.0, 5.3	100	48	1.2	8.9
PVBPA	5.23	2.7	58.3	0	12.3	34.5

[a] Measured using acid-base titration or calculated from equivalent weight; [b] Evaluated by solid-state ^{31}P NMR;
[c] Evaluated using interdigitated electrode arrays (IDAs). Note: The IEC of Aquivion® was 1.02 $mmol.g^{-1}$ and the IEC of Nafion™ was 0.91 $mmol.g^{-1}$. These values are based on their equivalent weight values provided by the manufacturer.

Our first set of experiments examined the ionomer blend compatibility when mixing the phosphonic acid ionomers with PFSA materials. **Figure 2a** shows pictures of the liquid ionomer solutions after blending at 2wt% for each solution. **Figures 2b** and **2c** are SEM-EDS map images and AFM images of PTFSPA and PTFSPA-Aquivion® blend spin-coated on silicon wafer substrates. The SEM-EDS map images identified phosphorus (i.e., the purple color) on film's surface. The images convey uniform phosphorus distribution across the studied area. Furthermore, the SEM-EDS of the element fluorine (color green) for PVPA-Aquivion® and PVBPA-Aquivion® blends are shown in **Figure S7**. These SEM-EDS images convey uniform distribution of the fluorine. SEM-EDS images were collected at three different places on the sample, and each image was similar. The AFM images of the phosphonic acid ionomer with Aquivion® are shown in **Figure 2c** and they also demonstrate that Aquivion® was not phase separated in the thin films of blended ionomers.

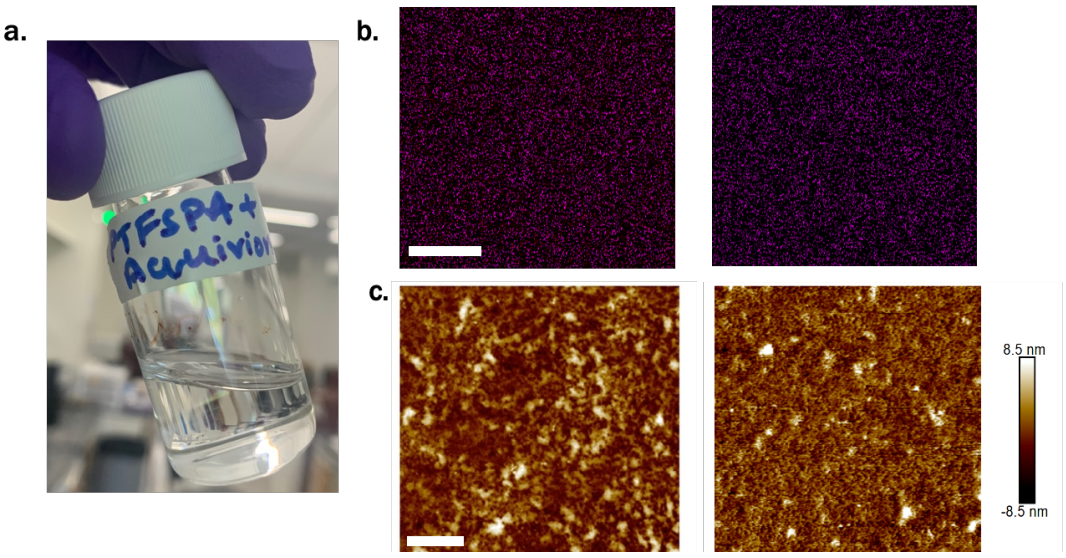

Figure 2. (a) Picture of ionomer blend of PTFSPA with Aquivion®; (b) SEM-EDX map of phosphorus in PTFSPA and the blend of PTFSPA with Aquivion®; (c) AFM images of the PTFSPA and the blend of PTFSPA with Aquivion®. The length of the white scale bars in (b) represents 1 μm and (c) represents 400 nm. The P-to-S ratio in the PTFSPA with Aquivion® is 1.56.

The next set of experiments examined the thin film proton conductivity of ionomers and ionomer blends on IDAs without thin film electrocatalysts as described in our previous work[27, 35]. The ionic conductivity was studied as a thin film because the ionomer binder in the porous electrodes is often a thin film (< 100 nm and closer to ~10 nm)[36] on the electrocatalyst-electrocatalyst particle support. Studying the ionomer materials as thin films alleviates the need to prepare mechanically robust, free-standing membranes of the PFSA-phosphonic acid ionomer blends. The proton conductivity experiments were performed under controlled temperature and dry nitrogen (i.e., 0% RH) as shown in **Figure S4c** and using equation **E.SI.2**[37] in the SI. **Figure 3a** compares the thin film ionic conductivity of PTFSPA, PVPA, PVBPA, Nafion™, and Aquivion® ionomers and PTFSPA-Nafion™ and PTFSPA-Aquivion® blends. There are a few salient observations seen in this Figure: 1.) The Nafion™ and Aquivion® ionic conductivity is very low at 0% RH and its negligible at temperatures higher than 100°C because the higher temperature and dry environment removed residual water from the PFSA materials – which is

needed to mediate proton conductivity. Furthermore, the conductivity of Nafion™ and Aquivion® at 100% RH does not increase substantially because PFSAs as thin films are known to have lower conductivity than the membrane[38] due to nano-confinement; 2.) PTFSPA has the highest ionic conductivity of the non-blended samples; 3.) Adding Nafion™ and Aquivion® to PTFSPA improved the ionic conductivity by about 150% and 250%, respectively at 150 °C; 4.) PTFSPA-Aquivion® gave the highest ionic conductivity of all the samples tested and was better than PTFSPA-Nafion™. Because of observations (4) in **Figure 3**, we decided to perform the remainder of the experiments with Aquivion® as the PFSA material to blend with phosphonic acid ionomers. Aquivion® has a shorter side chain compared to Nafion™ and a slightly higher IEC value. Both attributes improve proton conductivity under drier conditions.

It is important to note that there is a slight dip in conductivity observed at around 100 ˚C - 125˚C for some of the ionomer and ionomer blend materials. We attributed this to evaporation of residual water from the film in the temperature range. Water aids proton conductivity. To investigate this effect, we pre-treated the samples by exposing them to 200˚C for 15 minutes to drive off residual water. We then cooled the samples and measured the conductivity as a function of temperature. **Figure S4f** in the SI shows the conductivity measured after the thermal pre-treatment step. **Figure S4e** provides data without thermal pretreatment. Upon comparing **Figures S4e and S4f,** it is seen that the dip in conductivities around 100 ˚C has almost vanished by employing the thermal pre-treatment step. Future work will adopt this treatment protocol for probing the proton conductivity of thin films of high-temperature ionomers**.**

Figure 3b compares the proton conductivity of PVPA and PVBPA with and without Aquivion® added. Not only did the addition of Aquivion® enhance PTFSPA proton conductivity,

but it also increased the proton conductivity of PVPA and PVBPA. These materials, PVPA and PVBPA, by themselves, had very low proton conductivity. PVPA has very low ionic conductivity due to its propensity to form non-ionic, phosphate ester groups (i.e., anhydrides). PVPA is commercially available, and so is Aquivion®. Hence, researchers can use these commercial materials as electrode binders for HT-PEM electrochemical systems. PVBPA is derived from poly(vinyl benzyl chloride), which is much lower in cost and produced in much larger volumes when compared to poly(pentafluorostyrene).

Figures S4a and **S4b** in the SI shows the proton conductivity data for different phosphonic acid and PFSA blends with different phosphonic acid to sulfonic acid (P/S) ratios. These experiments identified the optimal blend composition for each blend system for the data presented in **Figures 3a** and **3b**. In the case of PTFSPA with Aquivion®, a P/S ratio of 1 to 2 gave the highest proton conductivity. For PVPA with Aquivion®, a P/S ratio of 2 to 5.28 gave higher proton conductivity values. However, a P/S ratio of 1 showed low proton conductivity.

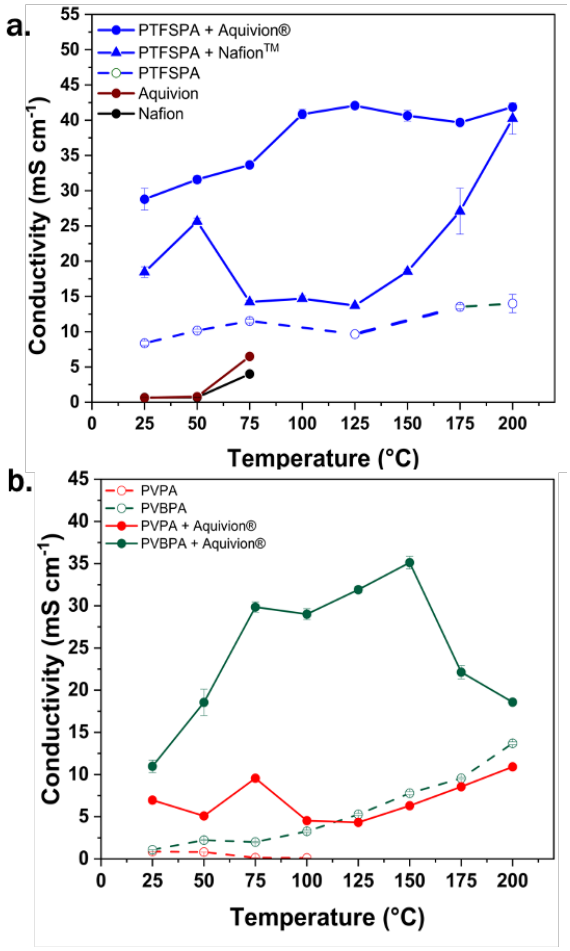

Figure 3. Thin film proton conductivity of ionomer and ionomer blends as a function of temperature: (a) PTFPSA, Nafion™, Aquivion®, and their blends; (b) PVPA, PVBPA, and their blends with Aquivion®. Error bars represent the standard error for n=3

Solid-state ^{31}P NMR was performed to measure the reduction in phosphate ester formation (i.e., anhydride formation) upon PFSA addition to the various phosphonic acid ionomers. Solid-state NMR was used as the characterization technique because it can discern phosphonic acid from phosphate ester and it allowed the blended samples to be processed as solids under the aggressive thermal annealing treatment of 250 °C for 5 hours under nitrogen to spur anhydride formation. Furthermore, it avoided solubility challenges that would inevitably arise from inter-chain crosslinking upon anhydride formation. **Figures 4a-c** correspond to the phosphonic acid ionomers before (red trace) and after thermal annealing (green trace). For the PVPA material only shown in

Figure 4a, the downward shift in the peak by 12 ppm found in ^{31}P NMR spectra signaled that all the phosphonic acid groups converted to phosphate ester upon thermal annealing. In the case of PVBPA and PVPA (**Figures 4b and 4c**), thermal annealing caused a large conversion of phosphonic acid to phosphate ester (58.3% and 100%, respectively). PTFSPA, on the other hand, showed a 21.2 % conversion of phosphonic acid to phosphate ester. Adding Aquivion® to the 3 different phosphonic acid ionomers (**Figures 4a-c**) mitigated anhydride formation completely upon the same thermal annealing treatment and drastically reduced anhydride formation by 48% in PVPA. **Table 1** lists the % of anhydride in the samples after thermal annealing of the phosphonic acid ionomers and phosphonic acid ionomers blended with Aquivion®.

The reduction in phosphate ester formation upon adding Aquivion® was attributed to the superacid nature of the PFSA material. Acids and bases can hydrolyze anhydrides to tethered anions that are dissociated. Furthermore, the proton in the sulfonic acid moiety of the PFSA can enhance the proton activity of the phosphonic acid group, which has been described as the protonation of the phosphonate by the sulfonic acid[28]. Mitigating phosphate ester formation and protonating phosphonate groups in phosphonic acid ionomers with the addition of Aquivion® accounts for the improved proton conductivity of phosphonic acid ionomers with Aquivion® observed in **Figure 3**.

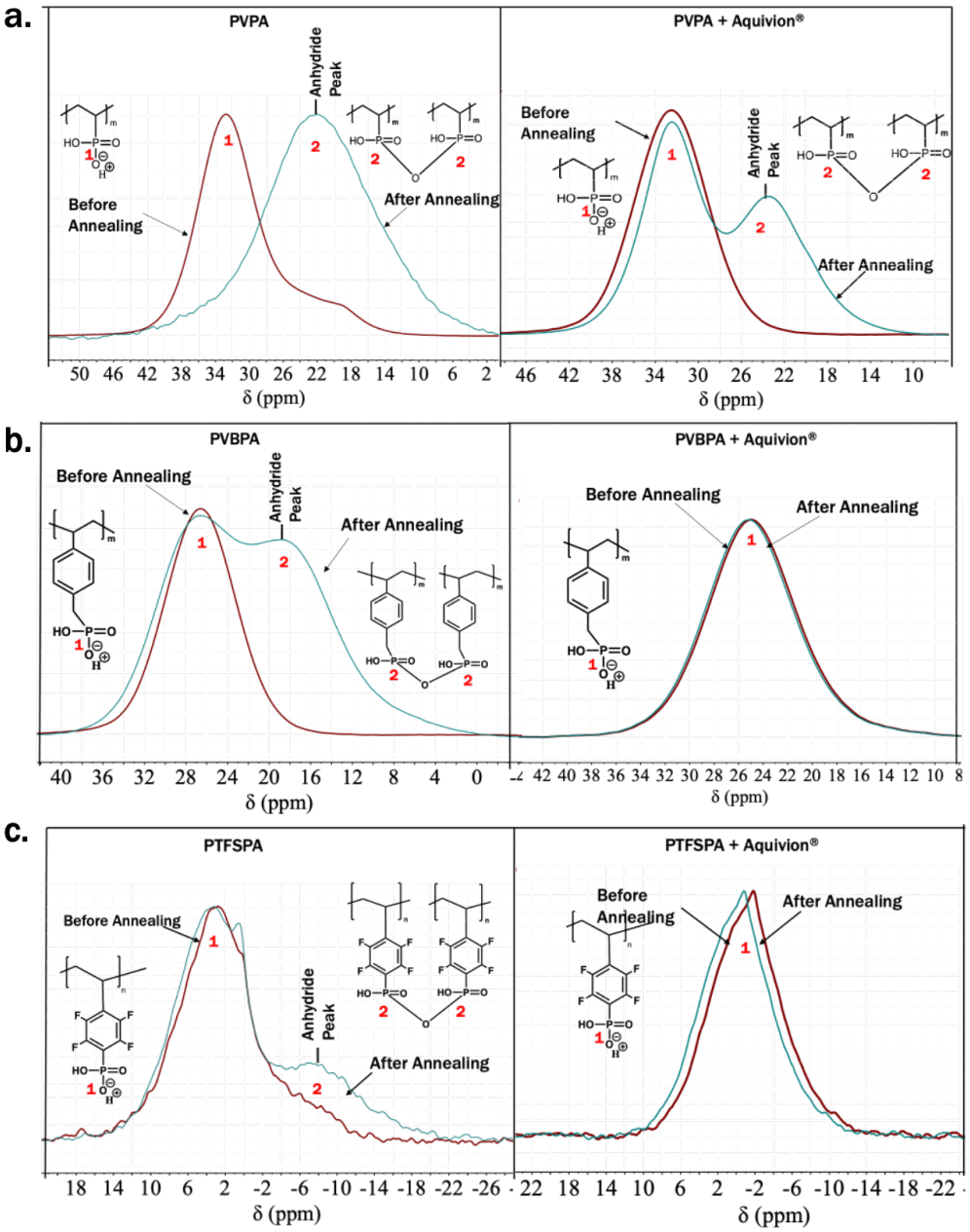

Figure 4. Solid State ^{31}P NMR spectra of (a) PVPA before and after annealing, a blend of PVPA and Aquivion® after annealing, (b) PVBPA before and after annealing, a blend of PVBPA and Aquivion® after annealing, and (c) PTFSPA before and after annealing, a blend of PTFSPA and Aquivion® after annealing.

The next experiments utilized IDAs decorated with nanoscale electrocatalysts prepared from block copolymer templates to determine how the ionomer and ionomer blend materials affect EHP polarization. These IDA chips, previously reported by us[35] and conveyed in **Figure 5a**,

allowed us to perform EHP experiments with thin films of PTFSPA and a polycation imbibed with phosphoric acid. The IDAs use 100x less platinum group metal loadings when compared to a standard 5 cm^2 MEA and do not require a bulk membrane separator. **Figure 5b** shows the IDA EHP polarization curves for PVPA, PVBPA, and PTFSPA, and the same phosphonic acid ionomers blended with Aquivion® at 200 °C and 0% RH. **Figure S8a** and **S8b** in the SI gives the polarization curves for the same materials at 120 °C and 160 °C. The P/S ratio of the phosphonic acid ionomer blended with PFSA which gave the highest proton conductivity was used for the EHP IDA studies. **Figure 5b**, and **Figures S8a** and **S8b**, demonstrate that the addition of Aquivion® to each of the phosphonic acid ionomer chemistry reduced EHP polarization.

The reduction in polarization with the addition of Aquivion® arises from improved HOR/HER kinetics and potentially improved hydrogen permeability. **Figure 5c** compares the IDA current density at a cell voltage of 1 V for the various ionomer and ionomer blend thin films. PTFSPA-Aquivion® provided the highest current density at 1 V and PTFSPA provided the second highest current density when used as a thin film electrolyte on the IDA. The current density at 1 V for the various temperatures was very low with PVPA and PVBPA ionomers as thin films. Adding Aquivion® to these two phosphonic acid ionomers improved the current density, but PVPA and PVBPA with Aquivion® showed lower current density values at 1 V when compared to the IDA with a PTFSPA thin film ionomer. We surmise that the large loading of phosphonic acid groups in PVPA and PVBPA compared to PTFSPA accounts for the lower HOR/HER kinetics when using PVPA and PVBPA. Adding Aquivion® reduces the number of phosphonic acid groups available in the phosphonic acid ionomers to adsorb to the nanoscale electrocatalysts. Plus, the fluorine moieties in the pentafluorostyrene ring of PTFSPA increase the acidity (shown later in DFT) resulting in improved HOR/HER kinetics. We also studied the PTFSPA-Aquivion® blended

ionomer at various P/S ratios on IDA decorated with Pt nanocatalyst. The results are reported in SI **Figure S8c**. We were able to see the same trends in the polarization data as obtained in the thin film proton conductivity measurements. Overall, the IDAs with and without nanostructured electrocatalysts allowed us to determine which thin film ionomer and ionomer blends gave the best ionic conductivity and the lowest EHP polarization – which encompasses HOR/HER kinetics and hydrogen gas transport. The trends observed in the IDA EHP studies correlated with the observations seen in MEA studies presented in the next section.

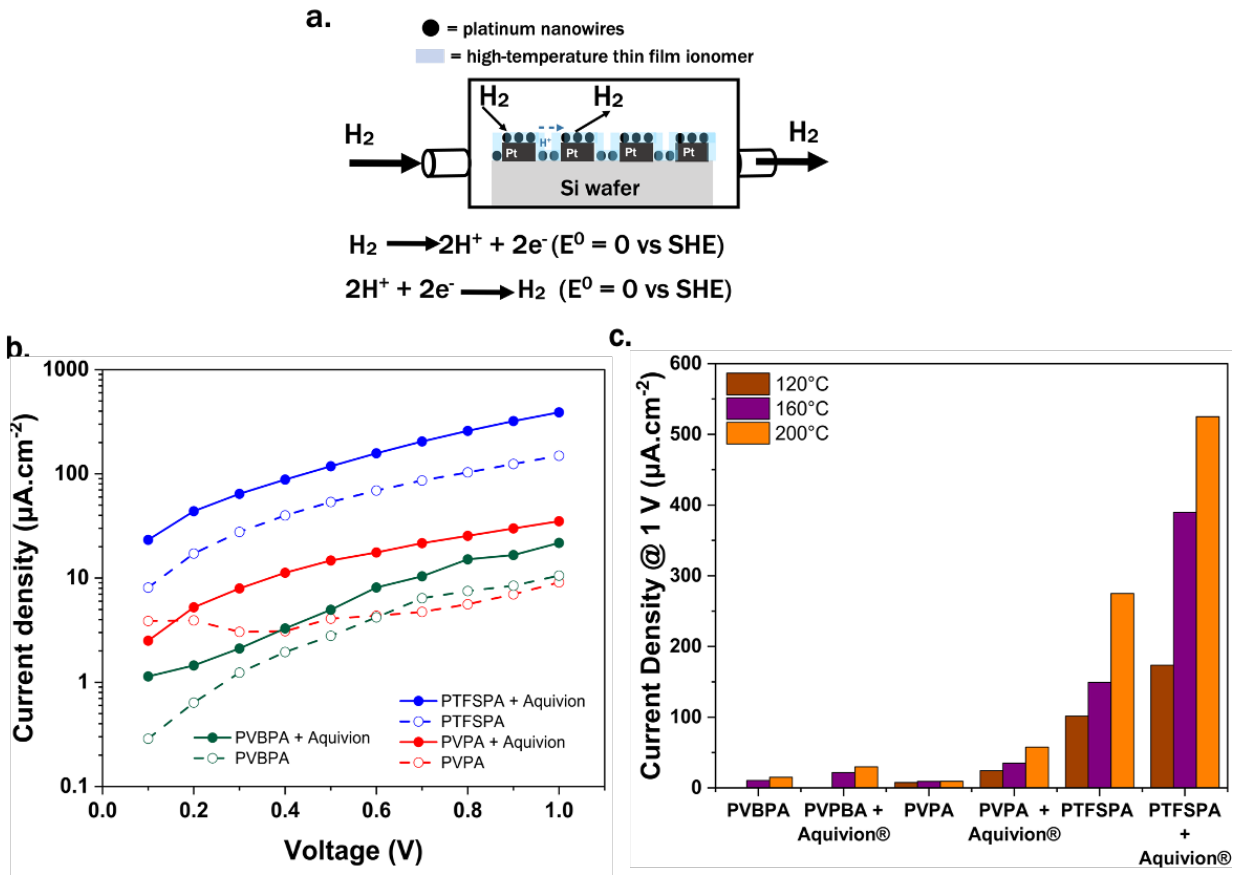

Figure 5. (a) IDA chamber showing the working of the hydrogen pump on an IDA. (b) Polarization curves of IDA hydrogen pump with different ionomers at 200 °C. (c) Summary of current density at 1 V as a function of temperature for the different thin film ionomers.

The final experiments assessed various ionomer and ionomer blend materials as electrode binders in a single-cell EHP. The MEAs with various ionomer binders used the same ion-pair HT-

PEM and gas diffusion electrodes (GDEs) – which consisted of 10 wt% of ionomer binder material with 1.0 mg_{Pt} cm^{-2}. The cell temperatures and anode feed gas flow rate with pure hydrogen (0.2 slpm) are the same for each MEA tested. In other words, these experiments examine how the electrode ionomer binder influences EHP polarization. **Figure 6a** gives the polarization curves of the EHP at 200 °C for the MEAs with different electrode ionomer binder materials. **Figures S9a** to **S9c** in the SI provide the polarization curves for the MEAs at 160 °C and 120 °C. Our primary focus has been to examine EHP polarization in MEAs and IDEs at 200 °C because the ion-pair HT-PEM and PTFSPA binder reported in our previous work was stable for 100 hours in the EHP device at that temperature and elevated temperature boosts HER/HOR kinetics, gas transport, and proton conductivity [20, 27]. The said effects result in less polarization. Conversely, we also examined the system at lower temperatures because lower temperature operation endows better durability of the cell components (e.g., the carbon support for the electrocatalyst). The key takeaways from **Figure 6a** are: 1.) The addition of Aquivion® reduced the polarization of the EHP, and this was especially significant when using PVPA and PVBPA binders because these binders by themselves manifested a limiting current with a small amount of cell voltage; 2.) The PVPA-Aquivion® had lower polarization when compared to PVBPA-Aquivion® despite PVBPA-Aquivion® having higher ionic conductivity as seen in **Figure 3b**; 3.) An EHP polarization curve of 5.1 $A.cm^{-2}$ at 0.4 V was attained with PTFSPA-Aquivion® binder – which is the highest value in the peer-reviewed literature (see **Table 2** for comparative literature results); and 4.) A reasonable EHP polarization curve, such as 2.25 $A.cm^{-2}$ at 0.5 V, could be attained with PVPA-Aquivion® - which are commercially available materials.

EIS was performed on the MEAs in an operating EHP to assess ohmic, charge-transfer, and diffusion resistances in the MEAs with the different binder materials. Prior to discussing

charge-transfer resistances, it is important to note that the high-frequency resistance (HFR) for all the MEAs at 200 °C was 0.045 to 0.050 Ω-cm^2 - which is a low value. **Figure 6b** and **Figures S9b** and **S9d** in SI provide the Nyquist plots with a background (DC bias) voltage of 0.05 V during EHP operation for the MEAs with different electrode binders. Using this background voltage resulted in a kinetically controlled EHP. The diameter values of the semi-circles in **Figure 6b** were used to determine the charge-transfer resistance (R_{ct}) values for HOR/HER with the different electrode binders in the MEAs (**Fig. 6c**). Adding Aquivion® to each of the phosphoric acid ionomers reduced R_{ct} and the reductions in R_{ct} were significantly greater for the PVPA and PVBPA systems when adding Aquivion®. At small background voltage biases, the R_{ct} is inversely commensurate to the exchange current density (i_o) – which is a proxy for the reaction rate coefficient for HOR/HER[39]. Hence, the addition of Aquivion® is shown to promote electrode kinetics.

Figure 6d is the Nyquist plot for the different MEAs with a background voltage of 0.75 V during EHP operation to assess the diffusion resistance for mass-transfer controlled EHPs. The limiting current occurred at 0.75 V for all the MEAs. The traces in **Figure 6d** show oblique lines in the low-frequency regime indicating a diffusion-controlled process. **Figure 6e** is the Warburg plot constructed from the low-frequency EIS data in **Figure 6c**. The calculated diffusion resistance (σ) from the slope of the lines is given in **Figure 6e**. The incorporation of Aquivion® with each of the phosphonic acid ionomers reduced σ by improving hydrogen gas diffusivity as σ scales to $D_{H2}^{-0.5}$. The corresponding Nyquist plots and calculated HFR values and R_{ct}, for the various MEAs tested in the EHP at 160 °C and 120 °C are given in **Figures S9** and **S10** in SI. The trends seen at 200 °C were qualitatively the same at 120 °C and 160 °C. Overall, MEA polarization curves and

Nyquist plots demonstrate that the addition of Aquivion® promotes electrode kinetics for HOR/HER and hydrogen gas transport.

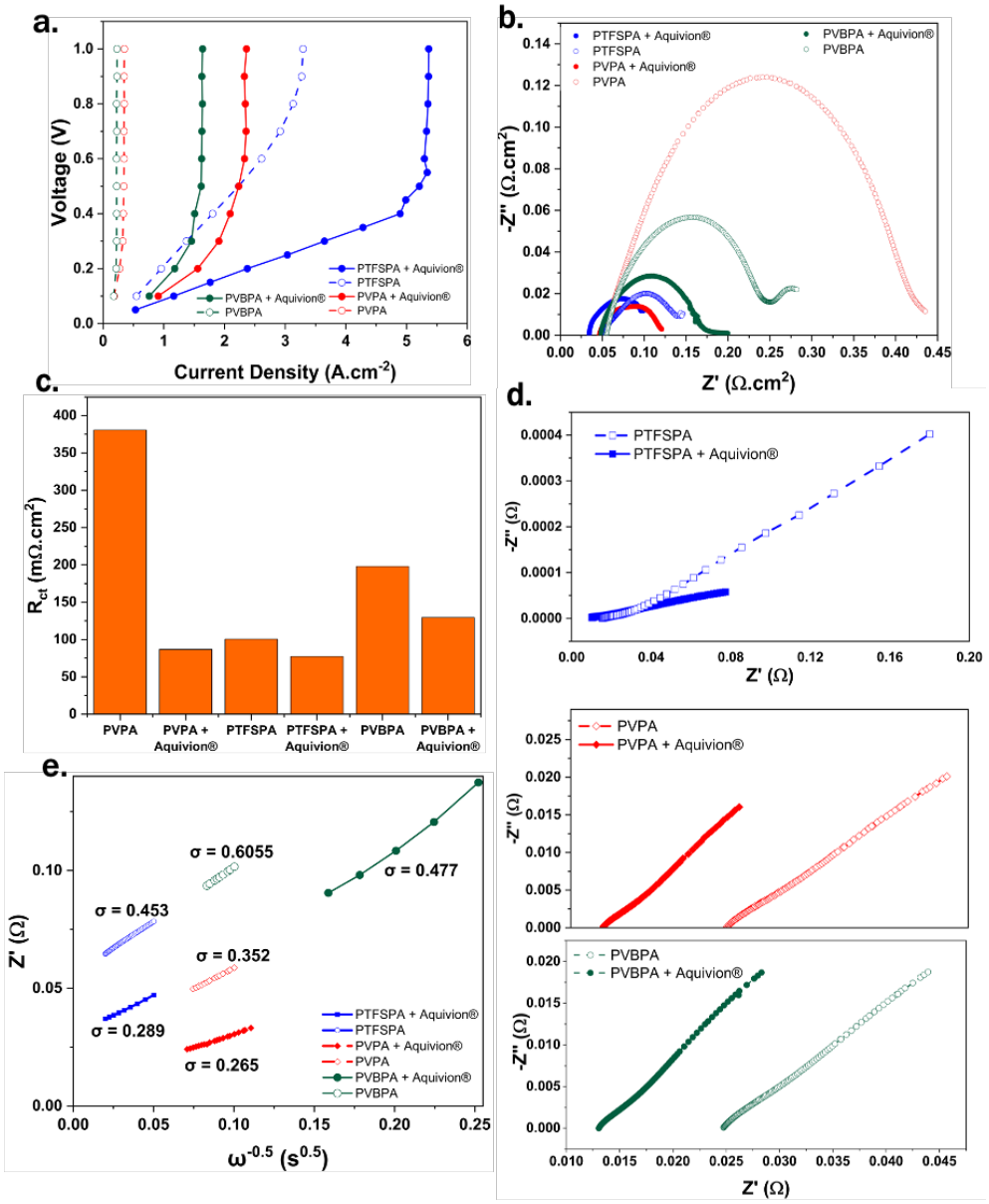

Figure 6. (a) MEA EHP polarization data at T = 200 °C with ion-pair HT-PEM, anode and cathode loadings of 1 mg_{Pt} cm^{-2} and different electrode ionomer binders (PTFSPA, PVPA, PVBPA with no Aquivion® and blended with Aquivion®). (b) EIS of the EHP at T = 200 °C with the different ionomer binders in the MEAs with a DC bias of 0.05V; (c) Charge transfer coefficient (R_{ct}) extracted from EIS with DC bias of 0.05V; (d) EIS of the EHP at T = 200 °C with the different ionomer binders in the MEAs with a DC bias of 0.75 V; (e) Warburg plot showing the diffusion resistance (σ) calculated from the Nyquist plots for MEAs with the different ionomer binders.

To test the durability or stability of EHP, a chronopotentiometric experiment was performed for 100 hours with the MEA containing PTFSPA-Aquivion® as the electrode binder. **Figure 7** provides the cell voltage as a function of time over 100 hours with a steady-state current hold of 1 A cm^{-2}. The durability experiment was performed at 200 C and with a pure hydrogen feed to the anode of the EHP. The final change in cell voltage was +4 mV over 100 hours. Overall, PTFSPA-Aquivion® as an electrode binder shows exceptional durability in HT-PEM EHPs.

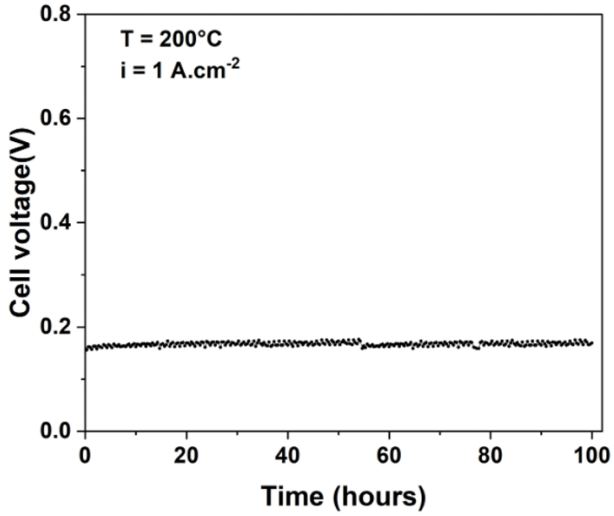

Figure 7. EHP stability test at 200 °C and a constant current of 1 $A.cm^{-2}$ with the blend of PTFSPA and Aquivion® as binder.

Table 2. Comparing HT-PEM EHP performance metrics in this report against literature data

Electrode/ binder type	**Membrane Used**	**Anode/Cathode PGM loading $mg_{Pt}cm^{-2}$**	**Temperature (°C)**	**Maximum current density achieved for the given voltage ($A.cm^{-2}$ /V)**	**Reference**
PTFSPA	PA doped QPPsf and PBI	0.5/0.5[a]	200	1.5/0.40	27
BASF electrodes that contain Pt	Para-PBI	1.0/1.0	200	1.0/0.13[b]	40

BASF electrode with Pt	PBI	1.0/1.0	180	2/0.21[b]	41
Etek electrodes with Pt	PBI	1.0/1.0	160	2.2/0.75	42
PBI with Pt/C	Fumatech PBI	-	160/0	2/0.35[b]	16
PVPA and Aquivion®	PA doped QPPsf and PBI	1.0/1.0	200	2.3/0.60	This work
PTFSPA and Aquivion®	PA doped QPPsf and PBI	1.0/1.0	200	5.1/0.40	This work

[a]For higher loadings the limiting current density values are not reported; [b]current densities for higher voltages are not disclosed.

To deconvolute the ohmic, activation, and concentration overpotentials in the EHPs, the experimental data obtained were iR corrected and fitted to a voltage loss breakdown model (SI section **SI 11.3**) to estimate the activation overpotential (η_{act}) and concentration overpotential (η_{con}) terms as a function of current density for a given temperature. These two overpotential terms plus the ohmic overpotential term (η_{ohm}) were added to obtain the predicted voltage (model). **Figure 8** shows that the voltage loss breakdown model fits the EHP polarization data at 200 °C for the MEAs with different electrode ionomer binders. The model fitting the data for 120°C and 160 °C is provided in **Figures S11 and S12** in SI. The dark squares circles represent the experimentally obtained data and the solid black lines represent the model output. We estimated the activation and concentration overpotential terms by fitting iR-corrected polarization data using equations **E.SI.3** and **E.SI.7** in SI. The ohmic overpotential was explicitly determined from the area-specific resistance, obtained from EIS. The activation, ohmic, and

concentration overpotential terms are plotted along the actual cell voltage for a given MEA with an ionomer binder type in **Figures 8a-f**.

The reduction in cell polarization when incorporating Aquivion® with the phosphonic acid ionomer electrode binder was primarily attributed to a reduction in activation overpotential and concentration overpotentials. The ohmic overpotential was also reduced, but not significantly as the membrane ohmic resistance dominates the ohmic overpotential in the MEA and the membrane was the same for each MEA. To illustrate this observation, consider the overpotential terms at 0.25 A cm^{-2} for PTFSPA and PTFSPA + Aquivion® as reported in **Figure 9a**. Most of the reduction in cell voltage is attributed to a reduction in activation and concentration overpotentials with the addition of Aquivion®, while the change in ohmic overpotential is small. In the case of PVBPA, we see a reduction in all three overpotentials; however, the activation and concentration overpotential reduction is more significant with the addition of Aquivion® when compared to the ohmic overpotential. For the case of PVPA, the ohmic overpotential is reduced to a greater extent than that of the other ionomers since it is more prone to anhydride formation at higher temperatures compromising its proton conductivity. Still, the concentration and activation overpotentials are significantly reduced when blending Aquivion® with PVPA. Furthermore, a similar trend was observed for overpotentials, at higher current density near the limiting current region, as shown in **Figure 9b**. Hence, all three phosphonic acid ionomers demonstrate significant reductions in concentration and activation overpotentials in an MEA EHP when blending Aquivion®. The reduction in concentration overpotential when adding Aquivion® is attributed to this ionomer's high gas permeability[34], which was observed by the reduction in diffusion resistance in **Figure 6e**. Regarding electrode kinetics, we'll show in the next section via DFT calculations that sulfonate groups in Aquivion®

have less affinity to adsorb to the platinum electrocatalyst surface when compared to phosphonate groups in phosphonic acid ionomers. Overall, the voltage loss breakdown modeling provided further evidence that adding Aquivion® enhanced electrode kinetics and gas transport in electrode layers leading to less EHP polarization.

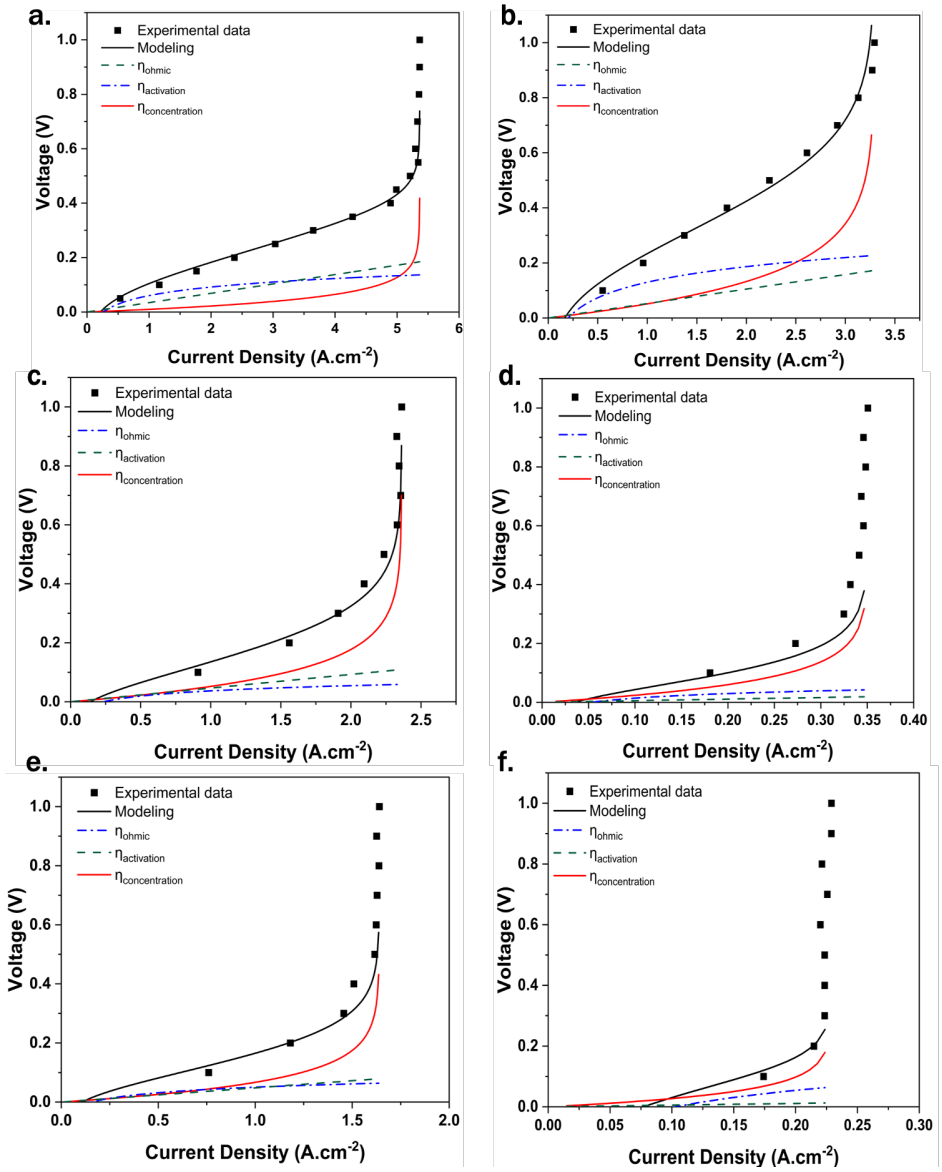

Figure 8. Polarization curve and modeling[29] of EHP data along with the breakdown of overpotentials (ohmic, activation, and concentration) at 200°C for (a) PTFSPA+Aquivion®, (b) PTFSPA, (c) PVPA + Aquivion®, (d) PVPA (e) PVBPA+Aquivion®,and (f) PVBPA.

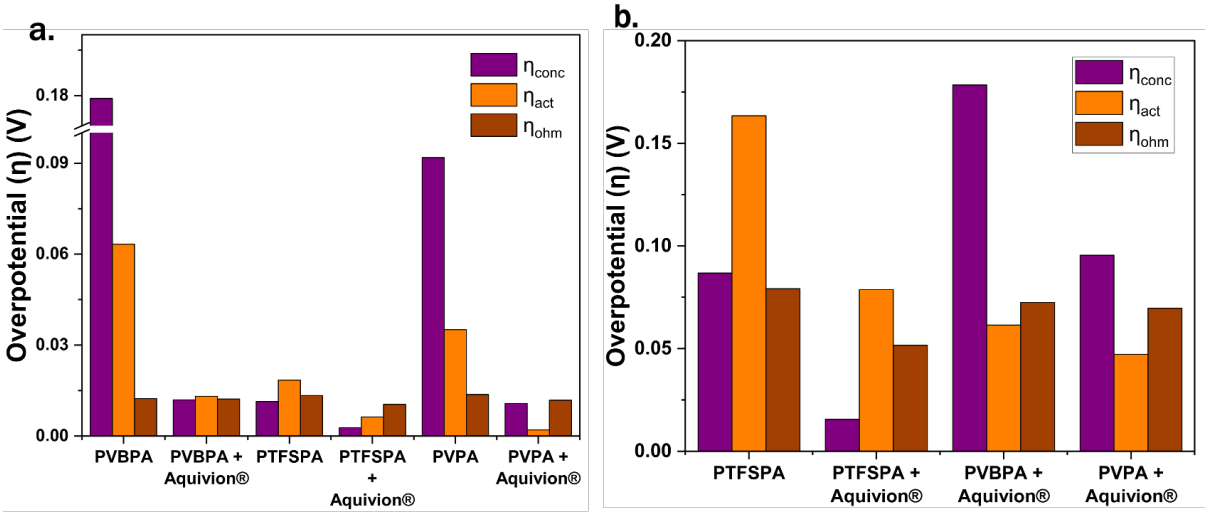

Figure 9. (a) Break down of the overpotentials of EHP at 0.25 A cm^{-2} or lower for 200 °C obtained from Figure 8. (b) Break down of the overpotentials of EHP near the limiting current density values at 200 °C obtained from Figure 8 (note: PVPA and PVBPA could not reach higher current densities and so those ionomers were not reported in b).

To further understand how the ionomer materials affected electrode activity and EHP performance, we employed density functional theory (DFT) calculations to probe how the ionomer functional groups, such as the different tethered anion chemistries, adsorb to platinum electrocatalysts. The DFT observations were related to experimentally measured R_{ct} values from EHP MEA studies. More specifically, the DFT results established a relationship between proton affinity (basicity of the anions of ionomers) and equilibrium adsorption potential of different adsorbed phosphate anions $RH_2PO_3^-$ relative to $H_2PO_4^-$ on Pt (111) surface. Previous work has shown that sulfate anions can adsorb on Pt (111) surface, inhibiting the activity of electrocatalysis[43], due to cations adsorbing on Pt[44]. DFT methods were used to determine a linear correlation between the equilibrium potential of adsorption and sulfate anion basicity, which can guide anion design to minimize anion adsorption and maximize electrochemical cell efficiency[43].

Specifically, it was shown that modulating the chain length and composition of sulfates varies the basicity of the anion and affects its tendency to adsorb on the Pt (111). The current study involves studying phosphate anion adsorption on the Pt (111) surface to determine any such linear trends.

The initial study involves equilibrium adsorption potentials with no solvation corrections relative to $H_2PO_4^-$ adsorption to provide insights as to how the ionomer materials in the electrodes may poison the electrocatalyst. Further, we have incorporated the implicit solvation effects having two different dielectric constants ($\varepsilon_r = 2$ and $\varepsilon_r = 6$) and compared the trend with no solvation correlations (**SI 12.4**). The qualitative trend remains the same for both the study.

Figure 10 shows a strong linear correlation between relative gas-phase equilibrium adsorption potentials and proton affinity of phosphate and sulfate anions on the Pt (111) surface. Gas-phase results in **Figure 10a** predict that the adsorption of phosphate anion adsorption can be tuned by varying the chain composition that affects the proton affinity (basicity) of the phosphate anion. Modifying the chain composition can increase both U_{NHE}^0 and proton affinity by up to 2.45 V vs NHE and 0.45 eV respectively in the gas phase.

The addition of an alkyl chain on phosphoric acid (PVPA) is predicted to decrease the favorability of anion adsorption of $PVPA^-$ relative to $H_2PO_4^-$ due to the increase in the equilibrium potential by 1.24 V-NHE and decreasing basicity. With the addition of a benzene ring complex, PVBPA is predicted to adsorb less favorably than PVPA due to an increase in the adsorption of equilibrium by 2.16 eV-NHE. Further, the addition of electron-withdrawing fluorine on the benzene ring of $PTFSPA^-$ is observed to decrease the basicity, resulting in an increase of U_{NHE}^0 = 2.45 V-NHE for $PTFSPA^-$ adsorption relative to $PVBPA^-$. Overall, the order of decreasing likelihood of adsorption of phosphate anions on Pt (111) surface ($H_2PO_4^- < PVPA^- < PVBPA^- < PTFPSA^-$) can be qualitatively predicted by the proton affinity of each anion. This agrees

qualitatively with experimentally observed R_{ct} resistance values (**Fig. 11**) as phosphate anions that adsorb more favorably would exhibit larger charge transfer resistance (R_{ct}) values.

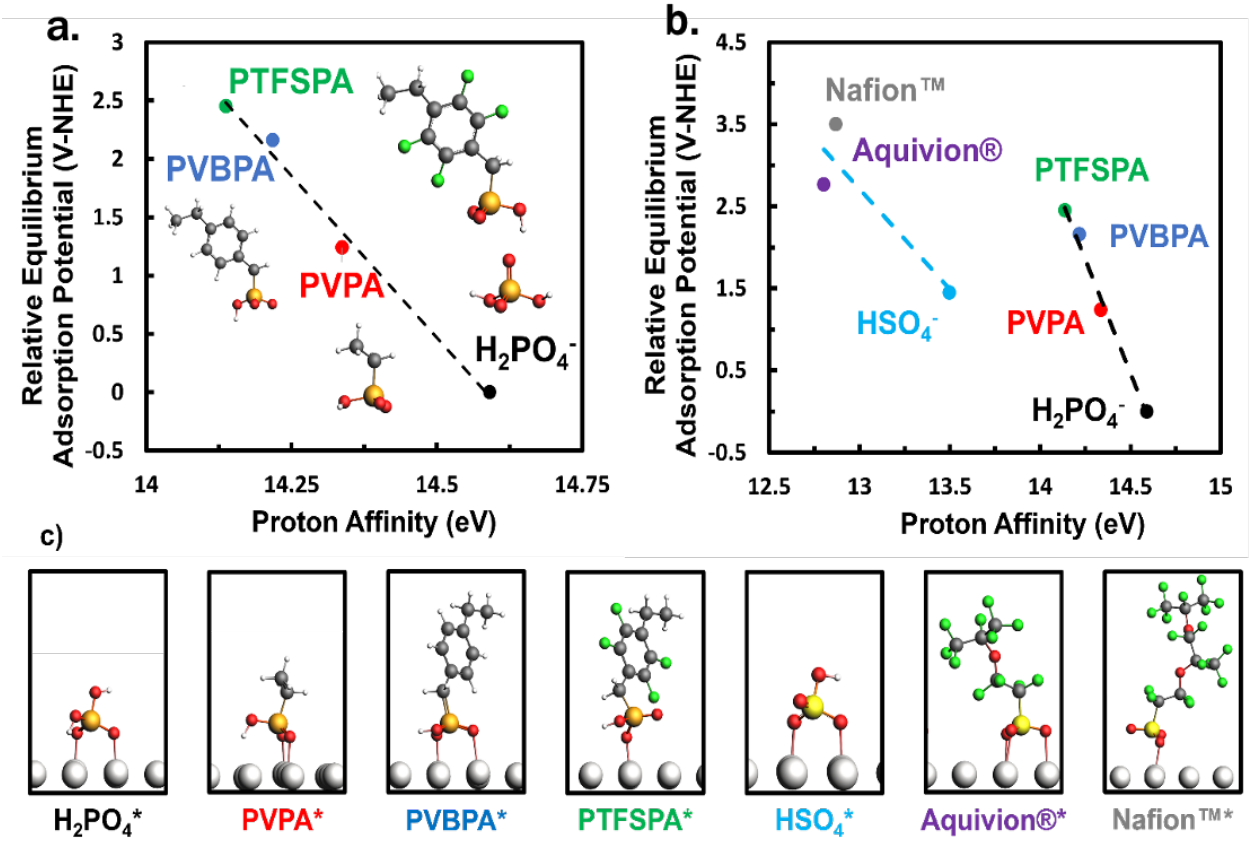

Figure 10. a) Linear correlation between relative gas-phase equilibrium adsorption potentials and proton affinities of phosphate anions on Pt (111) surface at 160 °C. U^0_{NHE} of different phosphate anions are relative to U^0_{NHE} of $H_2PO_4^-$ in the gas-phase. R^2 value of 0.99 was predicted for phosphate anions. b) Comparison between gas phase equilibrium adsorption potentials of phosphate and sulfate anions on Pt (111) surface w.r.t. proton affinities. All equilibrium potentials are relative to H_2PO_4*. Black lines indicate linear fit derived from phosphate anions while light blue linear fit is derived from sulfate anions. R^2 value of 0.82 was predicted for sulfate anions. c) Optimized geometries of both phosphate and sulfate monomers on Pt (111) surface are shown. Atom colors are as follows: Light grey = Pt, White = H, dark grey = C, Red = O, Orange = P, Green = F, and yellow = S.

The gas-phase equilibrium adsorption potential of phosphate anions is next compared with sulfate anions on Pt (111) surface relative to H_2PO_4* in **Figure 10b**. Gas-phase optimized

structures of sulfate anions are shown in **Figure S14.** DFT-predicted proton affinities predict that sulfate anions are less basic than phosphate anions with a difference of about one eV. Comparison between equilibrium potentials of phosphate and sulfates is not trivial to determine due to the uncertainties related to modeling ion solvation in bulk fluid and at the electrode-electrolyte interface. **Figure 10b** shows that Aquivion® is predicted to adsorb less favorably than the phosphate anions, where U^0 of Aquivion® is 1.52 V-NHE and 0.3 V-NHE more positive than PVPA and PTFSPA respectively. This may explain why blending phosphate anions with Aquivion®, a less basic anion, led to reduced activation overpotentials in the EHP experiment. The results presented in **Figure 10** are without solvation effects. **Figure S13** in SI shows the same DFT calculation incorporating implicit solvation. The linear correlation between equilibrium adsorption potentials and proton affinities of phosphates and sulfate anions is still maintained. We emphasize that modeling solvation and electrification within the DFT model limits to qualitative discussions related to the relative equilibrium adsorption potential of surface-bound anions. Further details regarding these challenges in quantifying the absolute adsorption potentials are discussed in SI 12.4.

Figure 11 shows the correlation between experimentally determined R_{ct} values and equilibrium adsorption potentials for different phosphate anions. The trend shows that with increasing propensity to adsorb (equilibrium adsorption potentials) the experimentally observed R_{ct} increases. DFT methods are useful in predicting the qualitative trends such as correlations between U^0 and proton affinities of both phosphate and sulfate anions and how tuning the chain composition of these anions would affect adsorption on the Pt (111) surface. DFT provides guidance on designing and developing new ionomers for EHP.

The DFT results were able to establish a correlation between the reaction kinetics in EHP and the propensity for the ionomer anion to adsorb on the platinum catalyst. This is an important finding to establish the effect of the ionomers on the reaction kinetics in the electrodes of EHP. With the blended ionomer of the phosphonic acid with Aquivion®, EHP polarization was reduced by lowering the activation overpotential. DFT provided molecular insights as to why the addition of sulfonic acid ionomers, like Aquivion®, reduces activation overpotentials – which are related to charge-transfer kinetics.

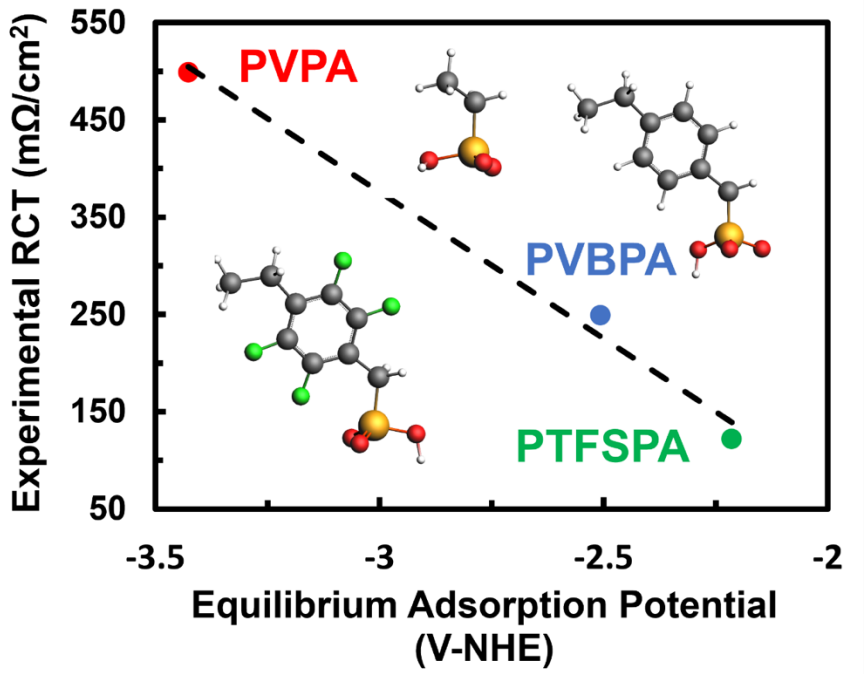

Figure 11. Correlation between gas-phase equilibrium adsorption potentials of phosphate anion adsorption on Pt (111) surface and charge transfer transfers at 160 °*C.* The R^2 value is 0.99. DFT optimized structures of gas phase phosphonic anions are shown. Atom colors are as follows: Light grey = Pt, White = H, dark grey = C, Red = O, Orange = P, and Green = F.

Conclusions

HT-PEM electrochemical systems have been around for about 30 years. Commercial variants of the MEAs for these systems have in the past primarily used PTFE as electrode binders followed by imbibing the porous electrode with phosphoric acid. Phosphonic acid ionomers blended with perfluorosulfonic acid ionomers are a new class of HT-PEM electrode binders. We show for the first time that adding a PFSA material, like Aquivion®, promotes reaction kinetics and gas transport in HT-PEM EHPs in addition to proton conductivity at 0% RH. Solid-state ^{31}P NMR showed that the addition of Aquivion® to a variety of phosphonic acid ionomer materials eliminated or significantly reduced phosphate ester formation (i.e., anhydrides) explaining why the Aquivion® addition improves proton conductivity under 0% RH. Electrode ionomer blends of PTFSPA with Aquivion® yielded an HT-PEM EHP that gives 5.1 A cm^{-2} at 0.4 V – the highest value in the literature. Furthermore, reasonable EHP performance (i.e., 1.5 to 2 A cm^{-2}) was attained with PVPA with Aquivion® and PVBPA with Aquivion® electrode ionomer blends. Using PVPA and PVBPA without Aquivion® as an electrode binder in a HT-PEM EHP resulted in no performance.

To further understand the role of the ionomer materials on EHP performance and electrode kinetics, we performed: i) EIS during EHP operation, ii.) voltage loss breakdown analysis to determine activation and concentration overpotential terms, and iii.) DFT to determine the extent of ionomer anion adsorption to platinum electrocatalysts. DFT revealed that sulfonate anions have less proton affinity than phosphonate anions, and that electron-withdrawing moieties adjacent to the phosphonate moiety in the phosphonic acid ionomer reduced the relative equilibrium adsorption potential to adsorb to platinum. Notably, an inversely commensurate relationship was observed between experimentally determined R_{ct} values from EIS and the relative equilibrium

adsorption potential to adsorb to platinum from DFT for the various ionomer materials. The voltage loss breakdown analysis and EIS revealed that adding Aquivion® to phosphonic acid ionomer binders reduced the charge-transfer kinetics and hydrogen diffusion resistance in the porous electrodes. In summary, a comprehensive approach of experiments and modeling at various length scales were combined to determine how the addition of Aquivion® to phosphonic acid ionomers improves EHP performance.

Methods

Materials

Pentafluorostyrene monomer, triethyl phosphite (TEP), petroleum ether, poly(vinyl phosphonic acid) (PVPA), and hexachloroplatinic acid were purchased from Sigma Aldrich and used as is. Sodium dodecyl sulfate, monosodium phosphate, potassium peroxydisulfate, dimethylacetamide (DMAc), and n-methyl-2-pyrrolidone (NMP) were obtained from Sigma Aldrich. DMAc and NMP were HPLC grade. Poly(vinyl benzyl chloride) (PVBCl) was purchased from Scientific Polymer Products. Trimethyl silyl phosphite was purchased from TCI Chemicals. Nafion™ and Aquivion® dispersions were purchased from Fuel Cell Store and were used as is. Poly(styrene-*block*-2-vinyl pyridine) (PS*b*PVP) block copolymers were purchased from Polymer Source Inc. and used as is. Si/SiOx wafers with 1 μm thick thermally grown oxide layer used in IDE manufacture were purchased from WRS Materials. Deionized water (DI) was withdrawn before use and was 18.2 MΩ. Deuterated solvents such as D6 DMSO and D8 THF were obtained from Sigma Aldrich.

Poly(pentafluorostyrene) synthesis

Pentafluorostyrene was polymerized using emulsion polymerization as described by Atanasov and co-workers[45]. An example reaction consisted of 100 mg (0.346 mmol) of sodium dodecyl sulfate and 10 mg (0.042 mmol) of monosodium phosphate dissolved in 10 g of deionized and degassed water in a 100 mL round bottom flask. 23 mg (0.95 mmol) of potassium peroxydisulfate was added to the mixture, stirred, and heated until dissolved. The round bottom flask containing the said components was then immersed in an oil bath heated to 100 °C. The headspace of the reaction vessel was blanketed with nitrogen and the flask was sealed. 5 g (25.8 mmol) of pentafluorostyrene was added to the reaction mixture with vigorous stirring from an overhead stirrer. The polymerization reaction occurred over 5 hours with constant stirring. Afterwards, the solution was cooled to room temperature and the solution was poured into isopropanol (100 mL) to precipitate the poly(pentafluorostyrene) polymer. The solid polymer was filtered and dried in a vacuum chamber. The polymer appearance was a white powder, and the yield was 4.6 g (i.e., 92% conversion of the monomer to polymer).

^{1}H NMR (500 MHz, THF-d8): δ (ppm) 2.1 (bp, 2H), 2.6 (bp, 1H).

GPC (eluent: THF, standard: polystyrene): M_n 57 kg mol^{-1}, M_w 92 kg mol^{-1}, PDI 1.614

Phosphonation of poly(pentafluorostyrene)

PTFSPA was prepared from poly(pentafluorostyrene) using the Arbuzov reaction[32]. 1 g (5.2 mmoles) of the synthesized poly(pentafluorostyrene) was dissolved in 4 g of dimethylacetamide (DMAc) at 170 °C. The reaction vessel was sealed and blanketed with nitrogen. 1.07 g (3.6 mmol) of tris-trimethylsilyl phosphite was added to the reaction vessel and the phosphonation reaction proceeded for 16 hours. After that, the PTFSPA solution was cooled and the PTFSPA was precipitated by pouring the polymer solution into 250 mL of boiling DI

water. The precipitated polymer was stirred in boiling DI water to hydrolyze the tethered phosphite to phosphonic acid. Then, the precipitated polymer was filtered, and it was rinsed in boiling water thrice for half an hour each time. Further, the polymer was boiled in 2 wt% phosphoric acid to convert the phosphonate ester into phosphonic acid form. After that, the polymer was filtered and washed with copious amounts of DI water until a filtrate pH of 6 to 7 was attained. The polymer was dried under a vacuum to obtain PTFSPA. The ^{31}P NMR spectrum in **Figure S1** in SI confirmed the presence of phosphonic acid in PTFSPA. Furthermore, the IEC of the synthesized PTFSPA was determined using acid-base titration and is reported in **Table 1**.

Phosphonation of PVBCl

Poly(vinyl benzyl phosphonic acid) (PVBPA) was prepared using the conventional Arbuzov reaction[46]. 1 g of PVBCl was dissolved in 22.5 ml of triethyl phosphite (TEP). The reaction vessel was sealed and heated to 120 ˚C. After 24 hours, the phosphonated polymer was precipitated in petroleum ether, filtered, and dried under vacuum at 80 ˚C to recover poly(vinyl benzyl phosphonate ester). The polymer was hydrolyzed to generate benzyl phosphonic acid tethered to the polymer backbone. The hydrolysis reaction was conducted by dispersing the poly(vinyl benzyl phosphonate ester) in concentrated hydrochloric acid (10 mL, 37%) and stirring it for 24 hours at 90 ˚C. After 24 hours, the polymer dispersion was cooled and gradually poured into an excess volume of DI water. The precipitated polymer was filtered and washed several times until the filtrate was pH 6 to 7. The collected PVBPA was dried under a vacuum at 60 ˚C. The ^{31}P NMR spectrum in **Figure S2** in SI confirmed the presence of phosphonic acid in PVBPA. **Table 1** reports the IEC of the synthesized PVBPA.

Electrochemical Testing

All the IDA experiments were conducted in a flow chamber with two electrical connections to measure the electrochemical properties of the ionomer materials. Note: The procedure for interdigitated electrode array (IDA) fabrication and IDA decorated nanoscale electrocatalyst synthesis is detailed in SI section **SI 10**. For thin film proton conductivity measurements, the ionomers were spin-coated on the gold-deposited IDA and loaded into the IDA chamber. The error bars in the thin film conductivity figure represent the standard error of the three measurements for each experiment.

For the EHP experiment, the ionomers were spin-coated on platinum-deposited IDAs decorated with platinum nanostructures. Prior to the experiment, the ionomer from the pads of the IDA was removed by using Q-tips to ensure proper electrical contact. The IDAs are spin-coated with the 2wt% of the ionomer of interest. The flow chamber passes either nitrogen (for conductivity experiments) or hydrogen (for EHP experiments). The IDA is equilibrated for 30 minutes under the passing gas before each experiment commences. All measurements were made using Gamry Potentiostat (3000AE). Galvanostatic EIS is performed for determining the in-plane film resistance. EIS experiments were performed with frequencies from 100,000 Hz and 1 Hz and with AC amplitude of 0.01 mA, by passing nitrogen for conductivity measurements. Chronoamperometry (from 0 to 1 V with an increment of 0.1 V) and EIS experiments (100,000 Hz and 1 Hz and with AC amplitude of 0.1 mA) were performed for the IDA hydrogen pump while passing hydrogen gas. The current density in the polarization curves shown in **Figure 6** was calculated by dividing the current obtained by the active area of the electrochemical cell in IDA (which is 0.0495 cm^{-2}).

For MEA EHP testing, a Scribner 850g test stand was used. All the experiments were conducted with a cell area of 4.3 cm^2. Gamry reference 3000 and Reference 30k Booster were used for the electrochemical measurements. Chronoamperometry (from 0 to 1 V with an increment of 0.05 V or 0.1 V) and EIS experiments (form 100,000 Hz and 1 Hz with 0.05V or 0.75V DC bias and 50 mA and 200 mA AC amplitude, respectively) were performed for the EHP testing.
The durability or stability test was conducted using a chronopotentiometry experiment under a constant current density of 1 $A.cm^{-2}$ over 100-hour duration.

Density Functional Theory methods and calculation

All DFT calculations in this work utilized the Vienna ab initio simulation package (VASP)[47-49]. The ionic cores are modeled using the projected augmented wave (PAW) method [50, 51]. The Perdew-Burke-Ernzerhof (PBE) generalized gradient approximation (GGA) exchange-correlation functional was used to approximate the electron-electron interactions[52, 53]. An energy cutoff used was 450 eV for convergence. A force criterion of 0.05 eV $Å^{-1}$ was used to ensure forces on the atoms converged to a minima during geometry optimization. A 20 Å periodic cubic cell was used to model isolated gas-phase molecules. A dipole correction in all directions (IDIPOL = 4) was utilized for all gas-phase calculations of molecules. A 3x3 FCC five-layer surface with 25 Å of vacuum was used to model the Pt (111) surface. The top two Pt layers were unconstrained to undergo surface relaxation. The bottom three layers were constrained to represent the bulk metal. Dipole corrections were implemented in the direction normal to the surface (IDIPOL = 3 and LDIPOL = .TRUE.) to prevent interactions between periodic cells. A 5x5x1 Monkhorst k- point grid was used to sample the Brillouin zone for Pt (111) surface [54]. The U_o is calculated based on the equations **E.SI.11** and **E.SI.12** shown in SI.

SEM and AFM

The BCPs and Pt nanostructures were observed under a field emission scanning electron microscope (G500 FESEM) using an operating voltage of 1 kV and a spot size of 3.5–4 nm while maintaining a working distance of 2–3 mm. AC mode AFM was performed using a Bruker Dimension Icon under Peak force tapping w/ ScanAsyst using uncoated Si Tip on Nitride layer (ACTA-SS, k = 0.4 N m−1, 115 μm length) operating at a resonant frequency of 70 kHz at a free amplitude of ≈650 nm. EDX images were taken using AztecLive Advanced Microanalysis System with UltimMax 100 SSD Detector connected to the Merlin FESEM. The operating voltage for this is 9 kV while maintaining a working distance of 7–8 mm.

Ellipsometry

The thickness of the ionomer thin film was determined using a Woollam M-2000F Focused Beam Spectroscopic Ellipsometer and modeled using Cauchy with an R^2 value of 0.97.

Gel permeation chromatography

The molecular weight of the polymer PPFS was analyzed by gel permeation chromatography (GPC) Tosoh HLC-8320 model with a built-in RI detector, with a flow rate of 0.35 mL/min. The column used is a Waters Styragel HR 5e. Additionally, our system is fitted with a Wyatt MALS detector. The concentrations used in our instrument range from 1 mg/mL to 5 mg/mL.

NMR spectroscopy

^{31}P Solid-State NMR spectroscopy was obtained from Brukner Avance-III-HD SS500 with magical angle spinning (MAS) rate of 12000 Hz and a resonance frequency of 202.36 MHz. High-power ^{1}H decoupling was applied during data acquisition, and cross-polarization mixing times of 2 ms were used for signal enhancement. Peaks were deconvoluted using Topspin software to obtain the area of the peaks. ^{31}P NMR experiments with liquid samples were carried out using Bruker AvanceVIII-HD-500 at a frequency of 202.484 MHz. Proton decoupling is employed to avoid doublet peak occurring in the spectrum.

Modeling EHP polarization data

The details about modeling the EHP polarization data from MEAs and IDAs are summarized in SI section **SI 11**.

Supporting Information

The Supporting Information contains NMR spectra of the phosphonated ionomers, thin film thickness data, IEC measurement procedure, thin film proton conductivity measurement procedure, and the data, SEM and SEM-EDX images, the procedure to prepare IDAs with decorated Pt electrocatalysts and EHP data with IDAs with Pt electrocatalysts, a chemical structure of the HT-PEM membrane used in the EHP system, additional EHP polarization results and modeling of polarization data, a comparison of EHP data in this report against data in the literature, IDA fabrication and nanoscale catalyst formation, details about modeling the EHP polarization data, and additional information about the DFT calculations for phosphate and sulfate anion adsorption on Pt (111) surface.

Acknowledgments

This material is based upon work supported by the U.S. Department of Energy's Office of Energy Efficiency and Renewable Energy (EERE) under the Advanced Materials & Manufacturing Technologies Office (AMMTO) Award Number DE-EE0009101. The views expressed herein do not necessarily represent the views of the U.S. Department of Energy or the United States Government. C.G. Arges also acknowledges support from the Electrochemical Society (ECS)-Toyota Young Investigator Fellowship and the National Science Foundation Award Number 2143056. We acknowledge the contribution of Penn State's Materials Research Institute, specifically Dr. Sarah Kiemle for training on AFM, Dr. Bangzhi Liu for helping with the SEM EDX, and Dr. Christy George for helping us with solid-state NMR. Special acknowledgment to Vincent Torres and Prof. Robert Hickey from the Material Science and Engineering Department at Penn State for performing GPC. We also thank Mr. Tanmay Kulkarni for reviewing the manuscript.

Author Contributions

K.A. performed all synthesis of the materials and experiments with materials; A.J.W.W. performed the DFT study with guidance from M.J.J.; L.B.M. performed the polarization modeling with guidance from J.A.R. H.E. assisted with EHP durability experiments. K.A., A.J.W.W., L.B.M., and C.G.A. wrote the manuscript. All authors contributed to the data analysis and editing of the manuscript.

Declaration of Interests

C.G.A. is a co-founder and owner of a startup company, Ionomer Solutions LLC, that is in the commercializing of HT-PEM and ionomer binder materials for HT-PEM EHP electrochemical systems.

References

1. M. R. a. P. R. Hannah Ritchie, CO_2 and Greenhouse Gas Emissions, https://ourworldindata.org/co2-emissions#global-co2-emissions-from-fossil-fuels-global-co2-emissions-from-fossil-fuels).
2. W. F. Lamb, T. Wiedmann, J. Pongratz, R. Andrew, M. Crippa, J. G. J. Olivier, D. Wiedenhofer, G. Mattioli, A. A. Khourdajie, J. House, S. Pachauri, M. Figueroa, Y. Saheb, R. Slade, K. Hubacek, L. Sun, S. K. Ribeiro, S. Khennas, S. de la Rue du Can, L. Chapungu, S. J. Davis, I. Bashmakov, H. Dai, S. Dhakal, X. Tan, Y. Geng, B. Gu and J. Minx, *Environmental Research Letters*, 2021, **16**, 073005.
3. A. Bhaskar, R. Abhishek, M. Assadi and H. N. Somehesaraei, *Journal of Cleaner Production*, 2022, **350**, 131339.
4. A. E. Yüzbaşıoğlu, A. H. Tatarhan and A. O. Gezerman, *Heliyon*, 2021, **7**, e08257.
5. S. Kharel and B. Shabani, *Energies*, 2018, **11**.
6. M. M. Catherine Ledna, Arthur Yip, Paige Jadun, and Chris Hoehne, Decarbonizing Medium- & Heavy-Duty On-Road Vehicles: Zero-Emission Vehicles Cost Analysis, https://www.nrel.gov/docs/fy22osti/82081.pdf).
7. F. T. Wagner, B. Lakshmanan and M. F. Mathias, *The Journal of Physical Chemistry Letters*, 2010, **1**, 2204-2219.
8. O. Gröger, H. A. Gasteiger and J.-P. Suchsland, *Journal of The Electrochemical Society*, 2015, **162**, A2605.
9. B. S. Pivovar, M. F. Ruth, D. J. Myers and H. N. Dinh, *The Electrochemical Society Interface*, 2021, **30**, 61.
10. K. R. Amgad Elgowainy , Ed Frank, Sheik Tanveer, H2 DELIVERY TECHNOLOGIES ANALYSIS, https://www.hydrogen.energy.gov/pdfs/review22/in025_elgowainy_2022_p.pdf).
11. M. Melaina, Hydrogen Delivery and Dispensing Cost, https://www.hydrogen.energy.gov/pdfs/20007-hydrogen-delivery-dispensing-cost.pdf).
12. J. Collis and R. Schomäcker, *Frontiers in Energy Research*, 2022, **10**.
13. K. Topolski, E. P. Reznicek, B. C. Erdener, C. W. San Marchi, J. A. Ronevich, L. Fring, K. Simmons, O. J. G. Fernandez, B.-M. Hodge and M. Chung, Hydrogen Blending into Natural Gas Pipeline Infrastructure: Review of the State of Technology, https://www.nrel.gov/docs/fy23osti/81704.pdf, DOI: 10.2172/1893355).
14. DOE, Blending Hydrogen into Natural Gas Pipeline Networks: A Review of Key Issues, https://www.energy.gov/eere/fuelcells/downloads/blending-hydrogen-natural-gas-pipeline-networks-review-key-issues).
15. Z. Hafsi, M. Mishra and S. Elaoud, *Procedia Structural Integrity*, 2018, **13**, 210-217.
16. K. A. Perry, G. A. Eisman and B. C. Benicewicz, *Journal of Power Sources*, 2008, **177**, 478-484.
17. N. A. Al-Mufachi, N. V. Rees and R. Steinberger-Wilkens, *Renewable and Sustainable Energy Reviews*, 2015, **47**, 540-551.
18. A. D. Kiadehi and M. Taghizadeh, *International Journal of Hydrogen Energy*, 2019, **44**, 2889-2904.
19. P. Rezaee and H. R. Naeij, *Carbon*, 2020, **157**, 779-787.

20. G. Venugopalan, D. Bhattacharya, E. Andrews, L. Briceno-Mena, J. Romagnoli, J. Flake and C. G. Arges, *ACS Energy Letters*, 2022, **7**, 1322-1329.
21. D. S. Maxwell, Q. Sun, H. Rojas, I. Kendrick, R. K. Pavlicek, E. S. De Castro, A. Aurora and S. Mukerjee, *Journal of The Electrochemical Society*, 2023, **170**, 034510.
22. J. M. Sedlak, J. F. Austin and A. B. LaConti, *International Journal of Hydrogen Energy*, 1981, **6**, 45-51.
23. G. Franchi, M. Capocelli, M. De Falco, V. Piemonte and D. Barba, *Membranes (Basel)*, 2020, **10**.
24. A. Rodrigues, J. C. Amphlett, R. F. Mann, B. A. Peppley and P. R. Roberge, 1997.
25. G. Venugopalan, K. Chang, J. Nijoka, S. Livingston, G. M. Geise and C. G. Arges, *ACS Applied Energy Materials*, 2020, **3**, 573-585.
26. K.-S. Lee, J. S. Spendelow, Y.-K. Choe, C. Fujimoto and Y. S. Kim, *Nature Energy*, 2016, **1**, 16120.
27. G. Venugopalan, D. Bhattacharya, S. Kole, C. Ysidron, P. P. Angelopoulou, G. Sakellariou and C. G. Arges, *Materials Advances*, 2021, **2**, 4228-4234.
28. K. H. Lim, A. S. Lee, V. Atanasov, J. Kerres, E. J. Park, S. Adhikari, S. Maurya, L. D. Manriquez, J. Jung, C. Fujimoto, I. Matanovic, J. Jankovic, Z. Hu, H. Jia and Y. S. Kim, *Nature Energy*, 2022, **7**, 248-259.
29. L. A. Briceno-Mena, G. Venugopalan, J. A. Romagnoli and C. G. Arges, *Patterns*, 2021, **2**, 100187.
30. L. Vilčiauskas, M. E. Tuckerman, G. Bester, S. J. Paddison and K.-D. Kreuer, *Nature Chemistry*, 2012, **4**, 461-466.
31. S. H. Kwon, S. Y. Lee, H.-J. Kim, S. S. Jang and S. G. Lee, *International Journal of Hydrogen Energy*, 2021, **46**, 17295-17305.
32. V. Atanasov, A. S. Lee, E. J. Park, S. Maurya, E. D. Baca, C. Fujimoto, M. Hibbs, I. Matanovic, J. Kerres and Y. S. Kim, *Nat Mater*, 2021, **20**, 370-377.
33. Y. J. Lee, B. Bingöl, T. Murakhtina, D. Sebastiani, W. H. Meyer, G. Wegner and H. W. Spiess, *The Journal of Physical Chemistry B*, 2007, **111**, 9711-9721.
34. S. Sambandam, J. Parrondo and V. Ramani, *Physical Chemistry Chemical Physics*, 2013, **15**, 14994-15002.
35. D. Bhattacharya, S. Kole, O. Kizilkaya, J. Strzalka, P. Angelopoulou, G. Sakellariou, D. Cao and C. Arges, *Small*, 2021, **17**.
36. M. Lopez-Haro, L. Guétaz, T. Printemps, A. Morin, S. Escribano, P. H. Jouneau, P. Bayle-Guillemaud, F. Chandezon and G. Gebel, *Nature Communications*, 2014, **5**, 5229.
37. D. Sharon, P. Bennington, C. Liu, Y. Kambe, B. X. Dong, V. F. Burnett, M. Dolejsi, G. Grocke, S. N. Patel and P. F. Nealey, *Journal of The Electrochemical Society*, 2018, **165**, H1028.
38. M. A. Modestino, D. K. Paul, S. Dishari, S. A. Petrina, F. I. Allen, M. A. Hickner, K. Karan, R. A. Segalman and A. Z. Weber, *Macromolecules*, 2013, **46**, 867-873.
39. D. Voiry, M. Chhowalla, Y. Gogotsi, N. A. Kotov, Y. Li, R. M. Penner, R. E. Schaak and P. S. Weiss, *ACS Nano*, 2018, **12**, 9635-9638.
40. F. Huang, A. T. Pingitore and B. C. Benicewicz, *ACS Sustainable Chemistry & Engineering*, 2020, **8**, 6234-6242.
41. M. Thomassen, E. Sheridan and J. Kvello, *Journal of Natural Gas Science and Engineering*, 2010, **2**, 229-234.
42. B. C. E. Benicewicz, Glenn A. ; Kumar, S. K.; Greenbaum, S. G, *Journal*, 2014.

43. K.-Y. Yeh, N. A. Restaino, M. R. Esopi, J. K. Maranas and M. J. Janik, *Catalysis Today*, 2013, **202**, 20-35.
44. I. T. McCrum, M. A. Hickner and M. J. Janik, *Journal of The Electrochemical Society*, 2018, **165**, F114.
45. V. Atanasov, M. Bürger, S. Lyonnard, L. Porcar and J. Kerres, *Solid State Ionics*, 2013, **252**, 75-83.
46. S. H. Kim, Y. C. Park, G. H. Jung and C. G. Cho, *Macromolecular Research*, 2007, **15**, 587-594.
47. G. Kresse and J. Furthmüller, *Computational Materials Science*, 1996, **6**, 15-50.
48. G. Kresse and J. Furthmüller, *Physical Review B*, 1996, **54**, 11169-11186.
49. G. Kresse and J. Hafner, *Physical Review B*, 1993, **47**, 558-561.
50. G. Kresse and D. Joubert, *Physical Review B*, 1999, **59**, 1758-1775.
51. P. E. Blöchl, *Physical Review B*, 1994, **50**, 17953-17979.
52. J. P. Perdew, K. Burke and M. Ernzerhof, *Physical Review Letters*, 1997, **78**, 1396-1396.
53. J. P. Perdew, J. A. Chevary, S. H. Vosko, K. A. Jackson, M. R. Pederson, D. J. Singh and C. Fiolhais, *Physical Review B*, 1992, **46**, 6671-6687.
54. H. J. Monkhorst and J. D. Pack, *Physical Review B*, 1976, **13**, 5188-5192.